OPEN ACCESS
Thermophysics & Energy ARTICLE

Air-cooled battery thermal management system integrated with bionic shark structures based on PEG1500/EG/BN/TPE flexible composite

Xin Xiao,* Wenqiang Xu, and Mengting Yao
*Correspondence: xin.xiao@dhu.edu.cn
Received: February 25, 2026; Accepted: July 17, 2026; Published Online: July 23, 2026; https://doi.org/10.59717/j.xinn-energy.2026.100182

GRAPHICAL ABSTRACT

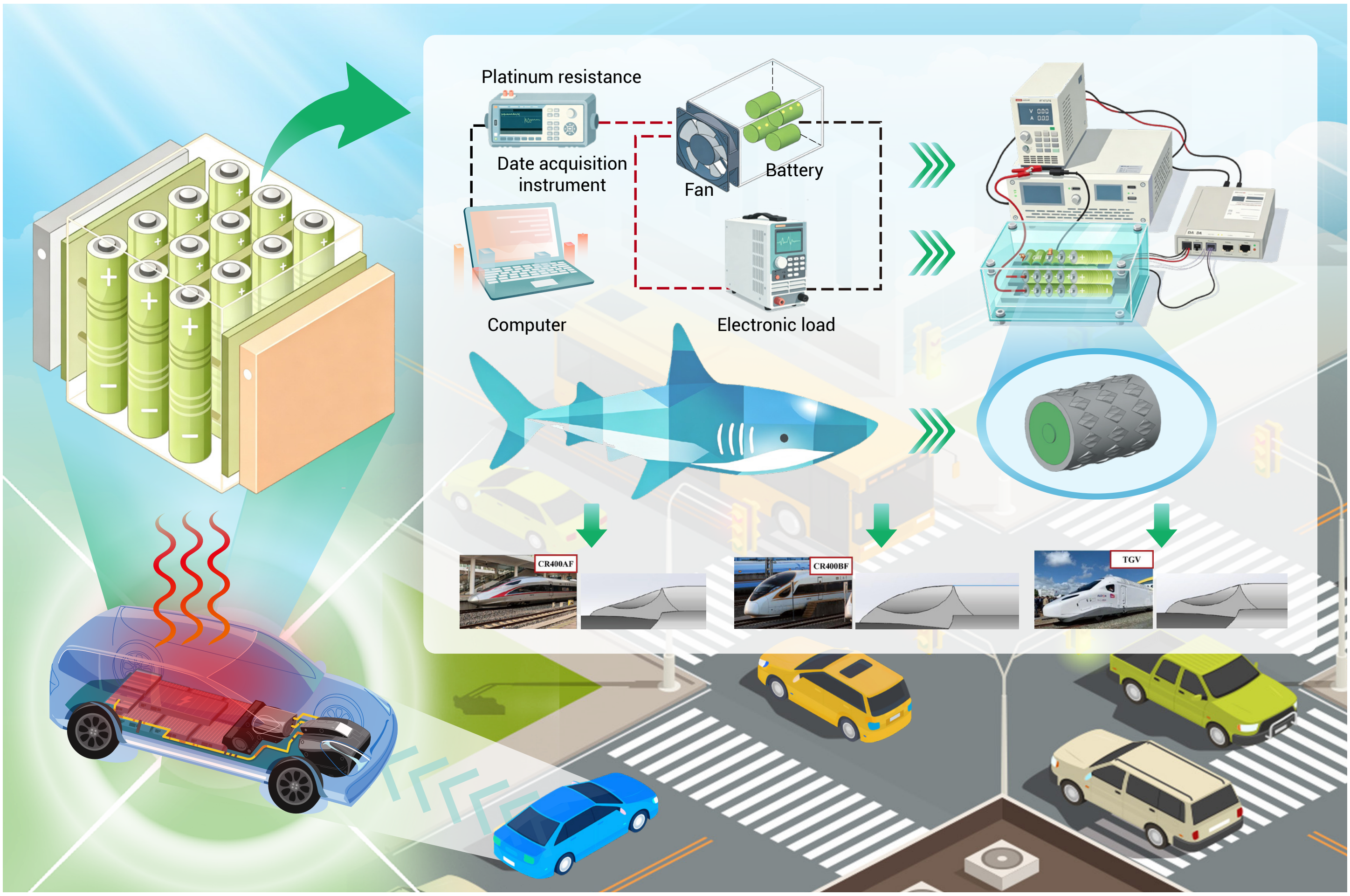

PUBLIC SUMMARY

- A bionic shark-scale structure optimizes composite phase change material (PCM) for electric vehicle battery thermal management system (BTMS) with axial air cooling.
- Four cooling modes and pressure drop tests are conducted; validated simulations explore the heat dissipation mechanism of bionic structures.
- Under 2C discharge, this hybrid scheme cuts temperature rise to 49.30% of natural convection and caps peak temperature at 50.90 °C.
- Multi-dimensional structural optimization achieves the best layout, lowering average battery temperature to 46.11 °C for BTMS heat sink design.

Air-cooled battery thermal management system integrated with bionic shark structures based on PEG1500/EG/BN/TPE flexible composite

Xin Xiao,* Wenqiang Xu, and Mengting Yao

College of Environmental Science and Engineering, Donghua University, Shanghai 201620, China

*Correspondence: xin.xiao@dhu.edu.cn

Received: February 25, 2026; Accepted: July 17, 2026; Published Online: July 23, 2026; https://doi.org/10.59717/j.xinn-energy.2026.100182

Citation: Xiao X., Xu W. and Yao M. (2026). Air-cooled battery thermal management system integrated with bionic shark structures based on PEG1500/EG/BN/TPE flexible composite. *The Innovation Energy* **3**:100182.

To improve the heat dissipation efficiency of electric vehicle battery thermal management system (BTMS), a bionic shark-scale structure was proposed to optimize the thermal performance of flexible composite phase change material (PCM), with axial air cooling integrated to regulate the battery temperature. Experiments were conducted under four conditions, i.e., natural convection, air cooling, air cooling coupled with PCM, and air cooling coupled with bionic shark-scale PCM, to evaluate the thermal behaviour performance. In addition, pressure drop tests were conducted to assess the drag-reduction effects of the bionic structures. A numerical simulation model was also built with the validation of experimental data, which was subsequently applied to investigate the heat dissipation mechanisms and influences of the bionic structure together with optimization. The results show that, under a 2C discharge, the temperature rise of the battery pack of air-cooled coupled with bionic shark-scale PCM is only 49.30% of that under natural convection, while the maximum surface temperature is controlled at 50.90 °C, ensuring the safe operation. At an airflow velocity of 1.30 m/s, the duct pressure drop of the bionic PCM is slight lower than that of the smooth PCM. Subsequently, the bionic shark-scale structure is further optimized in terms of axial aspect ratio, lateral structure, rib row number, and rib arrangement. The optimal configuration achieves an average battery pack temperature of 46.11 °C, with a fish scale aspect ratio of 0.5, a side structure of CR400AF, and 13 rows arranged in a cross pattern. The present research provides insights into the effective design of heat sink of BTMS.

INTRODUCTION

In recent years, the implementation of the dual-carbon policy has rendered green and low-carbon development to the strategic direction for all nationwide industries. To attain net-zero carbon emissions, the transformation of the energy structure has emerged as a primary task.[1] The automotive industry has likewise been in pursuit of practicable technologies to substitute fuel vehicles, aiming to drive the industry towards zero emissions. Electric vehicles are considered as a practicable technology to reduce the demand for fossil fuels.[2]

Energy storage system that can support high driving range and rapid charging capability is indispensable for electric vehicles.[3,4] Battery is the most widely used and crucial unit for energy storage in renewable energy ecosystems.[5] Lithium batteries possess advantages such as high energy density, longer cycle life, and shorter time-duration of charging, which leads to their extensive utilization in electric vehicles.[6] Nevertheless, during the vehicle operation, the battery undergoes discharging and generates a substantial amount of heat due to electrochemical reactions within it. The research has demonstrated that if the surface temperature of battery exceeds 50 °C, its cycle life and charged capacity would be significantly reduced.[7] Consequently, to maintain the safe operational temperature, an efficient battery thermal management system (BTMS) is essential to facilitate the dissipation of heat generated within the battery pack. Mainstream BTMS can be primarily classified into four main types: air-cooled BTMS,[8] liquid-cooled BTMS,[9] heat pipe BTMS,[10] and phase change material (PCM)-based BTMS.[11] The main limitations of air-cooled and liquid-cooled BTMS lie in their complex distribution systems and high operational energy consumption.[12,13] Heat pipe BTMS generally exhibits poor heat dissipation performance and significant temperature non-uniformity.[14] In contrast, PCM-based BTMS can reduce the system complexity while achieving the good temperature uniformity.[15,16] However, the traditional wrapping method results in the battery pack being heavy, which is not only detrimental to heat dissipation but impacts the energy density of battery pack. Relying solely on PCM, it is challenging to maintain the battery temperature within a safe range under extreme conditions. In addition to insufficient heat dissipation, recent reviews have emphasized that inadequate thermal regulation can significantly increase the risk of thermal runaway, and the rational structural design plays a critical role in enhancing both heat dissipation and safety of lithium batteries.[17]

Conventional PCM-based BTMS commonly depends on full wrapping of battery cells, which often results in excessive system mass and non-uniform heat dissipation, particularly for intermediate cells where heat accumulation is difficult to alleviate. In order to address these limitations, extensive efforts have been devoted to the material-level and structural optimization of PCM. Wu et al.[18] developed a composite PCM based on expanded graphite/paraffin/Fe_3O_4-modified graphene oxide, achieving a maximum battery temperature of 53.47 °C and a temperature difference of 3 °C under 3C discharge. Their results further indicated that, in addition to PCM composition, battery arrangement and PCM thickness were the critical parameters affecting thermal performances. Safdari et al.[19] investigated the influence of PCM package geometry and found that although rectangular packages exhibited the improved thermal performance under forced air cooling compared with circular ones, the battery temperature still exceeded 60 °C after a 2C charge–discharge cycle. Similarly, Alipanah and Li[20] reported that increasing PCM thickness within 7.5 to 15 mm delayed the temperature rise, yet excessive thickness introduced the structural vulnerability and limited further thermal enhancement.

Those studies collectively suggested that PCM optimization alone was insufficient to ensure the safe operation under long-term and high-rate discharge conditions. Experimental investigations further confirmed this limitation. Choudhari et al.[21] showed that even with an 8 mm PCM layer, the surface temperature of 18650 batteries under 3C discharge still reached approximately 85 °C, far beyond the safe operational range. Wu et al.[22] observed that PCM wrapping reduced the temperature rise at 3C and 5C discharge by 6 °C and 9.5 °C, respectively, yet overheating persisted without auxiliary cooling. Only by coupling PCM with fins and forced air cooling at an air velocity of 4 m/s could make the battery temperature control below 55 °C under 5C discharge, indicating that forced convection was indispensable for sustaining the effective heat dissipation.

In order to further enhance the convective heat transfer, structured PCM heat sinks were proposed to enlarge the heat transfer area and introduce additional airflow channels. Weng et al.[23] combined an aluminum honeycomb radiator with PCM and air cooling, achieving a 17.1% reduction in the maximum temperature of cylindrical battery packs at 4C discharge. Lv et al.[24] designed a serpentine PCM heat sink coupled with air cooling, which reduced the system mass by 70% and increased the energy density from 107.8 to 121.6 Wh/kg, while lowering the maximum battery surface temperature by 3.6 °C compared with conventional PCM wrapping. However, such highly structured PCM heat sinks inevitably introduce the increased flow resistance and might suffer from mechanical fragility, thereby constraining further enhancement of convective cooling under practical airflow conditions.

Under those circumstances, the thermal performance of PCM-assisted air-cooled BTMS becomes fundamentally limited not by latent heat capacity or heat transfer area, but by aerodynamic penalties imposed by flow resistance. From a broader perspective, recent studies on electrochemical energy systems have shown that surface and interface engineering can provide effective performance enhancement without increasing system complexity.[25] Therefore, surface structures capable of reducing the wall friction and regulating the near-wall flow behavior were of particular interest. Shark skin, characterized by regularly distributed rib-like protrusions and groove structures observed in scanning electron microscope (SEM) images, was widely recognized for its drag-reduction capability in high-density fluid environments.[26] Water tunnel experiments demonstrated that attaching genuine shark skin to the surface of a hollow elliptical tube significantly reduced the flow resistance over a wide velocity range.[27] Oeffner and Lauder[28] further showed that flexible membranes fabricated from real shark skin could increase the swimming velocity by an average of 12.3%, whereas artificial "shark-skin-like" fabrics failed to produce similar effects, highlighting the role of authentic surface geometry in near-wall flow regulation. Recent studies have already extended the drag-reduction concept to BTMS. Yang et al.[29] proposed a biomimetic shark-skin channel incorporating micro-riblet structures inspired by the shark skin and applied it to an axial air-cooling system. Experimental results demonstrated that the hybrid system significantly reduced both the peak and average temperatures of the heat source, while the bionic surface effectively suppressed flow separation, leading to a reduction in pressure drop. It was verified that shark-skin-inspired bionic structures provided a general advantage in simultaneously enhancing the heat dissipation and reducing the flow resistance across different cooling media, including air and liquid. Liu et al.[30] further applied scale-riblet microstructures derived from shark skin to channel design and proposed a bionic shark-skin channel (BSSC). The design integrated a diamond-shaped main channel with perpendicular sub-channels, where microstructures induced the localized turbulence to disrupt the thermal boundary layer while reducing the fluid-wall shear resistance. Through multi-objective optimization using the NSGA-II algorithm, the proposed structure achieved a 23.97% improvement in the temperature uniformity and a 22.62% reduction in the pump power, compared with conventional straight channels, demonstrating an outstanding drag-reduction-enhanced performance.

Despite the progress in PCM-based and hybrid air-cooled BTMS, two gaps still remain. Firstly, existing studies have mainly focused on PCM composition, thickness, or conventional heat-sink geometries, whereas the synergistic optimization of heat storage, convective heat transfer, and airflow resistance has been insufficiently addressed. Secondly, although shark-skin-inspired drag-reduction structures have shown promise in fluid channels, their integration with PCM heat sinks for BTMS has rarely been reported, and the underlying structural design parameters have not yet been systematically optimized for BTMS applications. Shark-scale structures are particularly suitable for PCM-based BTMS because they cannot only enlarge the effective heat transfer interface of the PCM heat sink but also regulate near-wall airflow and reduce flow resistance, which is critical for air-cooled battery packs where aerodynamic penalty can offset thermal benefits. In this way, a bionic shark-scale geometry provides a potential route to simultaneously improve the heat dissipation and lower duct pressure drop without introducing excessive system complexity. The present study proposes a heat sink of composite PCM optimized based on bionic structure and coupled with axial air cooling for BTMS, which can offer better capability of heat dissipation for battery pack. Initially, the composite PCM of heat sink with the structure of actual shark scales was used in the battery pack, and experiments and simulations of natural convection, air cooling, air-cooled coupled with composite PCM, and air-cooled coupled with bionic scale were conducted to investigate the heat dissipation of battery pack at 25 °C and discharge rates of 1C, 1.5C, and 2C. Subsequently, the bionic structure was optimized by adjusting the axial aspect ratio of shark scales, the lateral structure of shark scales, the row numbers, and the arrangement mode of shark scales, and the optimal structure of shark scales was finally explored.

MATERIALS AND METHOD

Battery packs and measurement apparatus

In the present study, the BYD 4680 lithium batteries (FC4680P, manufactured by Shenzhen BYD Lithium Battery Co., Ltd.) were used as the experimental samples. The parameters of the battery were summarized in Table S1. The diagrams of the BTMS are presented in Figure 1, where Figure 1A shows the schematic diagram of the system, Figure 1B shows the physical photo of the system. The experimental devices included an electronic load (DP3030, manufactured by Shenzhen Mestech Electronics Co., Ltd.), an Agilent data acquisition instrument (DAQ970A, manufactured by Keysite Technology (China) Co., Ltd.), a cooling fan (G12038HA2SL, manufactured by Delisi Electric Co., Ltd.), several calibrated T-type thermocouples, and four lithium batteries encapsulated in a rectangular duct. The batteries were discharged by means of the electronic load, with the batteries connected in a 4-series-1-parallel configuration. Temperature measurements were carried out using T-type thermocouples and the Agilent data acquisition instrument. The ambient temperature was regulated by an air conditioner and set at 25 °C. The thermocouples were axially positioned adjacent to the positive and negative electrodes of the battery as well as at the middle of the battery. The positive electrode of the cylindrical battery would have more pronounced heat generation. Figure 1C illustrates the front view of the thermocouple arrangement, and Figure 1D illustrates the side view of the thermocouple arrangement, where the thermocouples are exposed cell surface. At three positions of 135° and 315° on the upper right battery and 315° on the lower left battery, a total of 9 points of temperature measurement (A_1-A_9) were attached to compare the impacts of varying positions of duct on the heat dissipation performance of the battery.

The composite PCM used for the BTMS was independently developed,[31] which consisted of 68 wt.% PEG1500, 8 wt.% EG, 4 wt.% BN and 20 wt.% TPE. The preparation process included raw material mixing, heating and melting, uniform dispersion, providing good formability and flexibility. Differential scanning calorimetry (Mettler DSC1, METTLER-Toledo International Trading (Shanghai) Co., Ltd.) obtained its melting temperature as 43.83 °C, freezing temperature as 40.74 °C, and latent heat as 99.99 kJ/kg. In addition, the thermal conductivity of the composite PCM increased with temperature, reaching 1.780 W/(m·K), 1.802 W/(m·K), and 1.995 W/(m·K) at 27 °C, 42 °C, and 57 °C, respectively. The composite PCM was ground into powder, and the PCM heat sink was fabricated by pressing the powder in a tablet press at 6 MPa, after which it was attached to the battery. The axial profile of the bionic structure was obtained from the axial SEM images of shark scales presented in the study by Zhang et al.[27] The curve was fitted into a function using Origin software, and the function was then used to draw the structure in SolidWorks software. The height of the fish scale was determined to be 1.3 mm. Figure 1G illustrates the conceptual design of the bionic scale-structured heat sink, Figure 1H shows the customized pressing mould fabricated according to this structure, and Figure 1I presents the PCM heat sink constructed with the bionic scale pattern.

Experimental setup of pressure drop

The concept of shark-scale-inspired drag reduction has been extensively studied, and previous research has established the relationship between Reynolds number ratios and the drag-reduction efficiency of fish scales through the measurement of various parameters.[32] In the present study, a pressure difference sensor (LFM53, manufactured by Shenzhen Lifu Electronics Co., LTD., with an accuracy of 0.10 Pa) was placed at the inlet and outlet of the duct to reveal the impact sof different situations on the pressure drop, include non-wrapped PCM, wrapped smooth PCM, wrapped PCM of bionic scale. The pressure drop measurement system is shown in Figure 1E and Figure 1F. Figure 1E presents the schematic diagram of the pressure drop testing system, which mainly consists of the battery pack, fan, electronic load, differential pressure gauge, and air duct. Figure 1F shows the corresponding physical photograph of the experimental setup. The differential pressure gauge was connected to the pressure taps at the inlet and outlet of the duct to record the pressure drop during the battery discharge.

The measurement points for the pressure drop experiment were located at the mid-height of the side wall of the duct, positioned 7 cm apart between the positive and negative electrodes of the battery pack. Holes were drilled on the side wall of the duct using an electric drill, and the gauge pipes of pressure difference sensor were inserted into these holes. During the pressure drop experiment, the change in pressure drop was recorded throughout a 2C discharge of the battery pack.

The experimental uncertainty of the whole system mainly come from the accuracy of the differential pressure sensor, wire loss errors, fan speed, and PCM quality and thermophysical properties. The measurement accuracy of

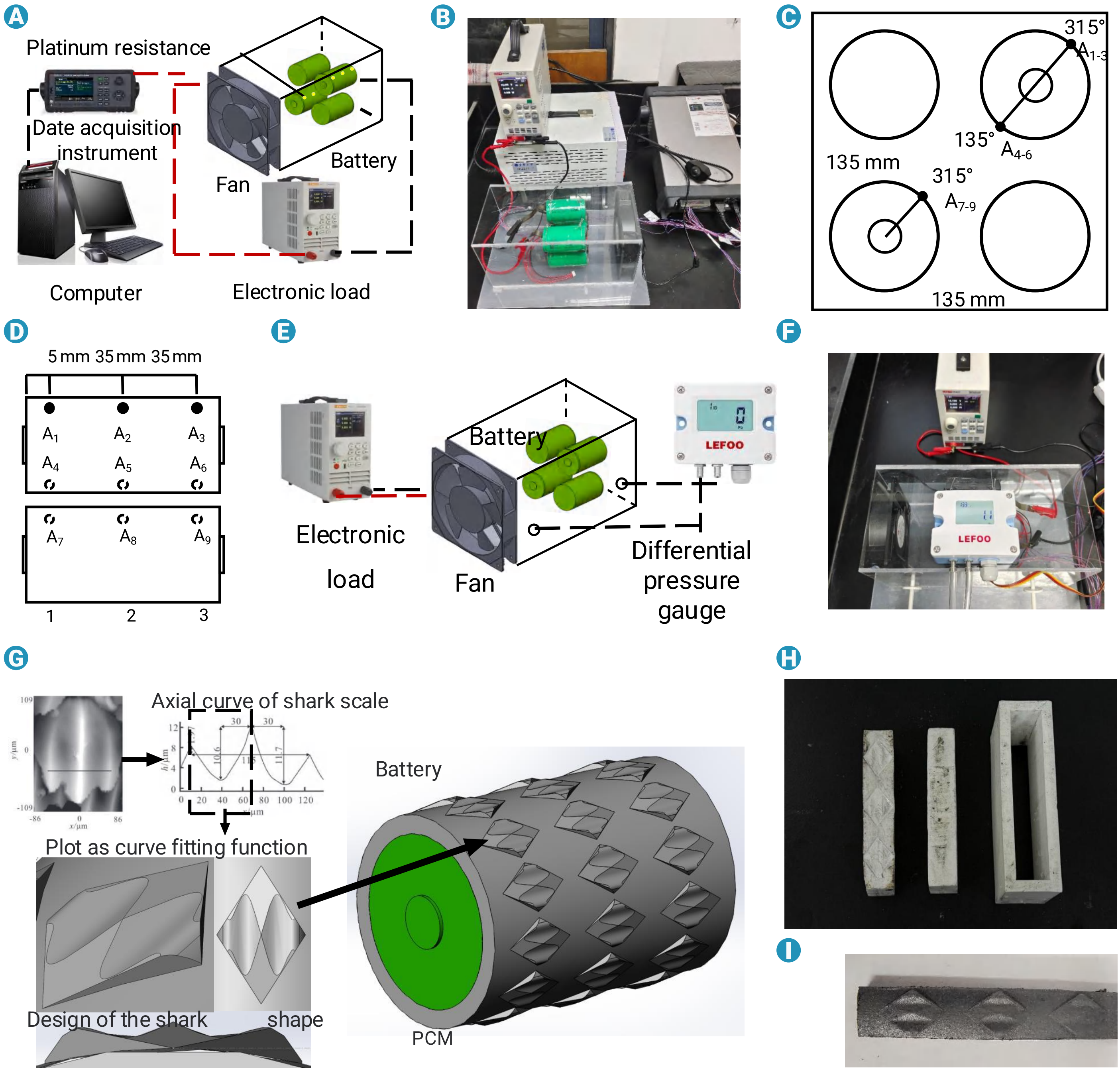

Figure 1. Whole BTMS: (A) Schematic diagram of BTMS; (B) Physical photograph of BTMS; (C) Front view of thermocouple arrangement; (D) Side view of thermocouple arrangement; (E) Schematic diagram of pressure drop system; (F) Physical photograph of pressure drop system. Schematic diagram of bionic heat sink: (G) Concept of heat sink of bionic scale structure; (H) Pressing mould; (I) Bionic heat sink of CPCM.

the differential pressure sensor is ± 2%, the uncertainty of wire loss is 1%/m, the uncertainty of the fan speed is ± 2%, and the uncertainty of the platinum thermal resistance is ± 1%. The measurement accuracy of the electronic balance is ± 1%. According to Equation (1), the total uncertainty of the inlet and outlet pressure drop testing system is within 3.32%.

$$\frac{\delta\Delta P}{\Delta P}=\sqrt{\left(\frac{\delta M}{\Delta M}\right)^2+\left(\frac{\delta Q_{Loss}}{Q_{Loss}}\right)^2+\left(\frac{\delta u_{fan}}{u_{fan}}\right)^2+\left(\frac{\delta T}{T}\right)^2+\left(\frac{\delta m}{m}\right)^2} \quad (1)$$

HPPC-based characterization of battery resistance

The resistance of lithium batteries is generally categorized into polarization resistance and ohmic resistance. Since the estimation of battery heat generation in the subsequent simulation is primarily determined by Joule heat during discharging, the measurement of battery resistance is considered crucial, as it directly affects the accuracy of the simulation results. In the present study, the hybrid pulse power characterization (HPPC) experiment was used to conduct a constant-rate pulse response on the battery under different states of charge (SOC), to obtain alterations of voltage and characteristics of resistance. The schematic diagram of voltage of HPPC experiment is shown in Figure S1A, while the experimental system of battery resistance is shown in Figure S1B. The typical HPPC experiment was as follows: Choosing A battery with a specific SOC was chosen, which was discharged at a constant 1C rate for 10 s and then rested for 40 s. Subsequently, the battery was charged at a constant 0.75C current for 10 s and rested for 40 s to complete a test cycle. During the charging and discharging processes, the step-like increase and decrease of the battery voltage, charging ohmic voltage ΔV_{c1} and discharging ohmic voltage ΔV_{dc1}, were attributed to the charge-transfer reaction at the interface between the electrode and the electrolyte, which was mainly ohmic resistance. The slow increase and decrease of the voltage, charging polarization voltage ΔV_{c2} and discharging polarization voltage ΔV_{dc2}, were attributed to the ion diffusion in the solid phase of the electrolyte, which was also the reason of the temperature rise and heat generation of the battery, named the polarization resistance [33]. However, in the actual testing process, the difference of the charge-to-discharge rate of the battery would lead to different ΔV_{dc1} and ΔV_{dc2}. Therefore, the HPPC method in current experiments measured the resistance of the battery under different discharge states, to ensure the accuracy of the experiment and subsequent simulations.

The calculations of the ohmic resistance and polarization resistance during charging and discharging are shown in Equations (2-I) - (2-IV), where R_{ec} and R_{edc} are the ohmic resistances during charging and discharging, and R_{pc} and R_{pdc} are the polarization resistances during charging and discharging, I_c and Idc are electric current during charging and discharging, respectively. During the experiment, the battery SOCs were set to 0, 0.20, 0.40, 0.60, 0.80, and 1, respectively, and three tests were carried out under each SOC for the purpose of accuracy.

$$R_{ec} = \Delta V_{c1}/I_c \tag{2-I}$$

$$R_{pc} = \Delta V_{c2}/I_c \tag{2-II}$$

$$R_{edc} = \Delta V_{dc1}/I_{dc} \tag{2-III}$$

$$R_{pdc} = \Delta V_{dc2}/I_{dc} \tag{2-IV}$$

Aspect ratio optimization of bionic shark scales

The structure of shark scale can reduce the flow resistance and enhance the heat dissipation effectively. The most prominent characteristic of the shark scale is regularly distributed with ridged protrusions and parabolic grooves on its surface,[34] as shown in Figure S2. The two-dimensional structure, aligned with the incoming flow of shark scales, closely resembles the concave parabolic rib used in heat transfer and also functions as a drag-reduction rib in fluid mechanics.[35] Concave parabolic ribs related to drag reduction is mainly due to diverse of the longitudinal flow and the transverse flow.

The starting height difference Δh (Δh = h_{pl} - h_{pc}) between the longitudinal flow and the transverse flow is a crucial factor affecting the transverse flow, as illustrated in Figure S3. It was concluded that the maximum possible difference Δh between the heights of the two ribs was Δh = 0.132s, where s is the lateral rib spacing. Consequently, as s increases, the Δh rises accordingly. Due to the effect of enhanced obstruction of the longitudinal ribs on the transverse flow, the fluctuation of the transverse flow near the surface would be mitigated, and the associated momentum exchange and resistance would also be decreased. The increase in the thickness of the viscous sub-layer corresponds to a decrease in the shear stress difference $\Delta\tau$ between the concave parabolic plate and the smooth plate. This reduction would lead to a decrease in the resistance of the concave parabolic rib test plate, and the quantitative relationship[35] between the height difference Δh and the initial slope of the drag reduction curve is as follows:

$$\frac{\Delta\tau}{\tau_0} \propto \frac{\Delta h}{s} s^+ \tag{3-I}$$

$$s^+ = \frac{s u_\tau}{v} \tag{3-II}$$

$$u_\tau = (\tau_0/\rho)^{0.5} \tag{3-III}$$

Where s^+ denotes the Reynolds number of the concave parabolic surface. v represents the kinematic viscosity, s is the rib spacing, m, u_τ is the wall friction velocity of the smooth plate under the same flow conditions, τ_0 is the shear stress on the concave parabolic plate, and $\Delta\tau$ is the difference of shear stress between the concave parabolic plate and the smooth plate. A negative value of $\Delta\tau/\tau_0$ corresponds to drag reduction. In addition, the relationship between the dimensionless fluid velocity u^+ and the wall friction velocity u_τ is shown in Equation (4), where the average Nusselt number Nu of the fluid swept plate and the Reynolds number Re are calculated with Equations (5) & (6).

$$u^+ = u/u_\tau \tag{4}$$

$$Nu = 0.664 Re_L^{1/2} Pr^{1/3} \tag{5}$$

$$Re = \rho u + l/\mu \tag{6}$$

As a consequence, when u_τ decreases of drag reduction, leading to an increase in u^+, and both Re and Nu increase. The physical significance of Nu is a parameter that quantifies the intensity of coefficient of the convective heat transfer of the fluid.

Numerical simulation of battery thermal behavior

Simplified model of battery heat generation. A commercial software of Ansys Fluent was used for the modeling, and the heat and variable coefficient of the convective heat transfer of the battery were realized through an interpretive user defined function. To simplify the model, the battery heat generation was only set to resistance heating, and the equation for calculation is as follows:

$$Q = I^2 R_{pdc} \tag{7}$$

Where Q represents the total battery heat generation, I is the electric current, R_{pdc} is the polarization resistance during battery discharge.

The total battery heat generation is divided by the volume of the battery core to obtain the volumetric heat source for the core. The calculation is expressed as follows:

$$q = Q/V \tag{8}$$

Where q represents the volume heat source of the battery core, V is the core volume of the battery.

Coefficient of convective heat transfer. The natural convective heat transfer on the outer surface of the battery was influenced by the temperature of incoming flow and the coefficient of convective heat transfer. The incoming flow temperature was set at room temperature 25 °C, and the coefficient of convective heat transfer was determined by Equations (9-I)-(9-III).

$$h_{wall} = \lambda_{air} \frac{Nu}{l} \tag{9-I}$$

$$Nu = c(Gr \cdot Pr)^n \tag{9-II}$$

$$Gr = \frac{g l^3 \beta \Delta T}{v^2} \tag{9-III}$$

The convective heat transfer of the battery was approximately taken from the form of a transverse cylinder, and the flow state was turbulence. In Equation (9-II), c = 0.1, n = 0.33. β is the volume expansion coefficient, λ_{air} is the thermal conductivity of air, the kinematic viscosity v and the Prandtl number Pr are obtained by consulting the book of Heat Transfer.[36] The size l is set to 80 mm, and g represents the gravity acceleration. It should be noted that the empirical correlation was only used to predict the equivalent convective heat transfer coefficient for the bare battery surface under natural convection. Considering the air-cooled cases with smooth or bionic PCM heat sinks, the local flow and heat transfer over the structured PCM surface were directly resolved by the CFD model through the governing equations, rather than being predicted by the empirical cylinder correlation.

Governing equations. Since the model involved the battery heat generation, PCM phase transition and natural convection processes, the governing equations were as follows:

The continuity equation is shown in Equation (10):

$$\frac{\partial\rho}{\partial t} + \nabla\cdot(\rho\overline{V}) = 0 \tag{10}$$

The momentum equations are shown in Equation (11):

$$x: \frac{\partial(\rho u)}{\partial t} + \nabla\cdot(\rho\overline{V}u) = \nabla\cdot(\mu\overline{V}u) - \frac{\partial P}{\partial x} \tag{11}$$

$$y: \frac{\partial(\rho v)}{\partial t} + \nabla\cdot(\rho\overline{V}v) = \nabla\cdot(\mu\overline{V}v) - \frac{\partial P}{\partial y} \tag{12}$$

$$z: \frac{\partial(\rho w)}{\partial t} + \nabla\cdot(\rho\overline{V}w) = \nabla\cdot(\mu\overline{V}w) - \frac{\partial P}{\partial z} \tag{13}$$

The energy equation is shown in Equation (14):

$$\frac{\partial(\rho T)}{\partial t} + \nabla\cdot(\rho\overline{V}T) = \nabla\cdot(\frac{\lambda}{c_p}\nabla T) - \frac{S_T}{c_p} \tag{14}$$

Modeling of PCM thermal behavior. The thermal conductivities of composite PCM in solid and liquid states are presented in Figure S4A. The heat capacity of PCM during the phase change was realized by the enthalpy model, and the latent heat was represented by the variety of apparent specific heat capacity with temperature. The apparent specific heat capacity of the material is shown in Figure S4B. In order to simplify the heat storage and release processes and improved the simulation efficiency, the following assumptions were adopted in the BTMS simulation:

(1) The thermal properties of the battery remained unchanged during charging or discharging.

(2) The effects of external radiation between the batteries and their surroundings were neglected during the experiments.

(3) The composite PCM exhibited a good shaping effect, and its subsequent flows after melting were confined during the experiment and could be neglected.

(4) The ambient temperature was kept constant at 25 °C.

The thickness of PCM is about 5 mm, and the Reynolds number based on the air velocity was calculated to be 11236, so turbulent flow model was used in the simulation process. Both *k*-eplison and *k*-omega models were used to simulate the process in a preliminary study, and it was found that *k*-eplison model was more suitable, which is similar to the reported air cooling BTMS.[37]

The energy equation for the PCM was as follows:

$$\rho\frac{\partial H}{\partial t} = \lambda\frac{\partial^2 T}{\partial x^2} \tag{15}$$

The total specific enthalpy *H* was the sum of sensible heat and latent heat, and was expressed as follows:

$$H = \int_{T_0}^{T} c_p dT + L\gamma \tag{16}$$

$$\begin{cases} L = 0 T < T_s \\ L = \frac{T-T_s}{T_l-T_s} T_s < T < T_l \\ L = 0 T > T_l \end{cases} \tag{17}$$

Where ρ is the density, λ is the thermal conductivity, H is the total enthalpy, T_0 is the temperature at which the enthalpy value is 0 kJ/kg, L is the liquid phase fraction, γ is the latent heat, and T_s and T_1 are the freezing and melting temperatures of the PCM, respectively.

RESULTS AND DISCUSSION

Experimental analysis of battery thermal behavior

Battery discharge performance. The experiment was carried out to test the battery under four distinct experimental configurations include natural convection, air cooling with a flow velocity of 1.3 m/s, air-cooled coupled with PCM, and air-cooled coupled with PCM of bionic scales, three distinct discharge conditions include 1C, 1.5C, and 2C. And the entire experiments were replicated twice to ensure the reliability and reproducibility of the results.

Figure 2A-D presents the schematic diagram of temperatures of each measuring point, which are under diverse experimental configurations of the battery during 2C discharge. The temperature variations for other conditions of 1C and 1.5C are shown in Figure S5. Table S2 summaries the final temperatures of battery after the discharge experiments. The slight difference in the time required to reach 50 °C between the air-cooled coupled PCM case and the air-cooled coupled bionic PCM case is mainly caused by the minor experimental fluctuations and the data recording interval. The battery temperature can reach 50.54 °C under the condition of natural convection of 1C discharge, while it can reach up to 77.51 °C during the 2C discharge. In the actual operation, batteries are highly susceptible to failure due to thermal runaway. When an air-cooled system is integrated into the battery pack, its heat dissipation performance is enhanced, and the temperature during 1C discharge eventually stabilizes at 43.36 °C. However, the temperature still rises to 57.17 °C during 2C discharge. Subsequently, the self-developed PCM was incorporated into the air-cooled battery pack, resulting in a maximum temperature of only 52.91 °C during 2C discharge. Finally, when the bionic-structured PCM is integrated with the air-cooling system, the maximum temperature of the battery pack during 2C discharge is further reduced to 50.90 °C, nearly reaching the safe operational range of battery.

Furthermore, the influences of the ducts on the temperature distribution across various locations on the battery surface are also examined. Figure 2E&F shows the final temperature and velocity of each point at different positions of duct. In the experiment of natural convection of 2C discharge, the six temperature measuring points A_1 - A_6 attached to the upper right battery all comply with the rule of the highest temperature at the positive electrode and the lowest at the negative electrode. The temperatures of the three points A_4-A_6, located at 135°, are slightly lower than the three points A_1-A_3 at 315°. It is assumed that the phenomenon could be attributed to two factors. Firstly, it could be due to the lower vertical height of A_4-A_6, so the air temperature within the duct is also lower than that of A_1-A_3, consequently leading to the temperature slightly reduced at the A_4-A_6. Secondly, it might be due to the uneven internal heating or heat transfer induced by manufacturing processes and other inherent issues of the battery, particularly the apparent temperature difference between A_3 and A_6. In the air-cooled experiment, the temperature at A_1 is higher than A_4, and the temperature difference between A_3 and A_6 is reduced. Considering the implementation of air cooling, it is assumed that the observed phenomenon could be attributed to the differences in velocity at various positions within the duct. Therefore, a numerical simulation for the velocity was performed, with the measuring points positioned 5 mm outside each point. The simulation results indicate that the flow velocity of A_1 and A_3 is faster than A_4 and A_6, which might make the temperature of A_1 higher than A_4, but the temperature difference between A_3 and A_6 become smaller.

Pressure drop of air duct. As shark scales benefit to reduce the flow resistance, so the structure of shark scale is integrated with the surface of the PCM for the purpose of conducting the experiments of battery discharge. The maximum temperature of the battery pack is found to be slightly lower compared to that of the smooth PCM. The phenomenon might be attributed to the factor that the structure of the shark scale reduces the flow resistance and enhances the heat dissipation of the battery pack. Therefore, the relevant experiments were carried out through the pressure drop test device. During 2C discharge, variations in the duct pressure drop were recorded in real time using a pressure difference sensor. Under the condition of air cooling with a flow velocity of 1.3 m/s, three sets of experiments were established, i.e., non-wrapped PCM, wrapped smooth PCM, wrapped PCM of bionic scale. Each experiment was repeated three times, and the the curves in the following figure represent the averaged measurements.

The outcomes of the three sets of experiments are presented in Figure S6, and the experimental data are summarized in Table S3. It can be seen from the experimental results that, the battery pack without PCM has the most spacious duct, resulting in the lowest pressure drop of the air duct. After wrapping the PCM, the pressure drop of the bionic PCM was reduced by 3.1% compared with the smooth PCM. The decrease in the pressure drop of the bionic PCM is in line with the relevant research,[33-35] and the energy efficiency could increase by about 4% with the bionic structure.

Battery internal resistance. In the present study, HPPC tests were carried out on battery at 1C, 1.5C, and 2C discharge rates for different SOC values of 0, 0.2, 0.4, 0.6, 0.8, and 1.0. Each set of experiments was repeated three times to obtain the average values. The variations of voltage when SOC equaled 1 are shown in Figure S7. The transition of the test voltage of the battery is greater when the SOC at full charge is 1.0 and the SOC at low charge is 0,

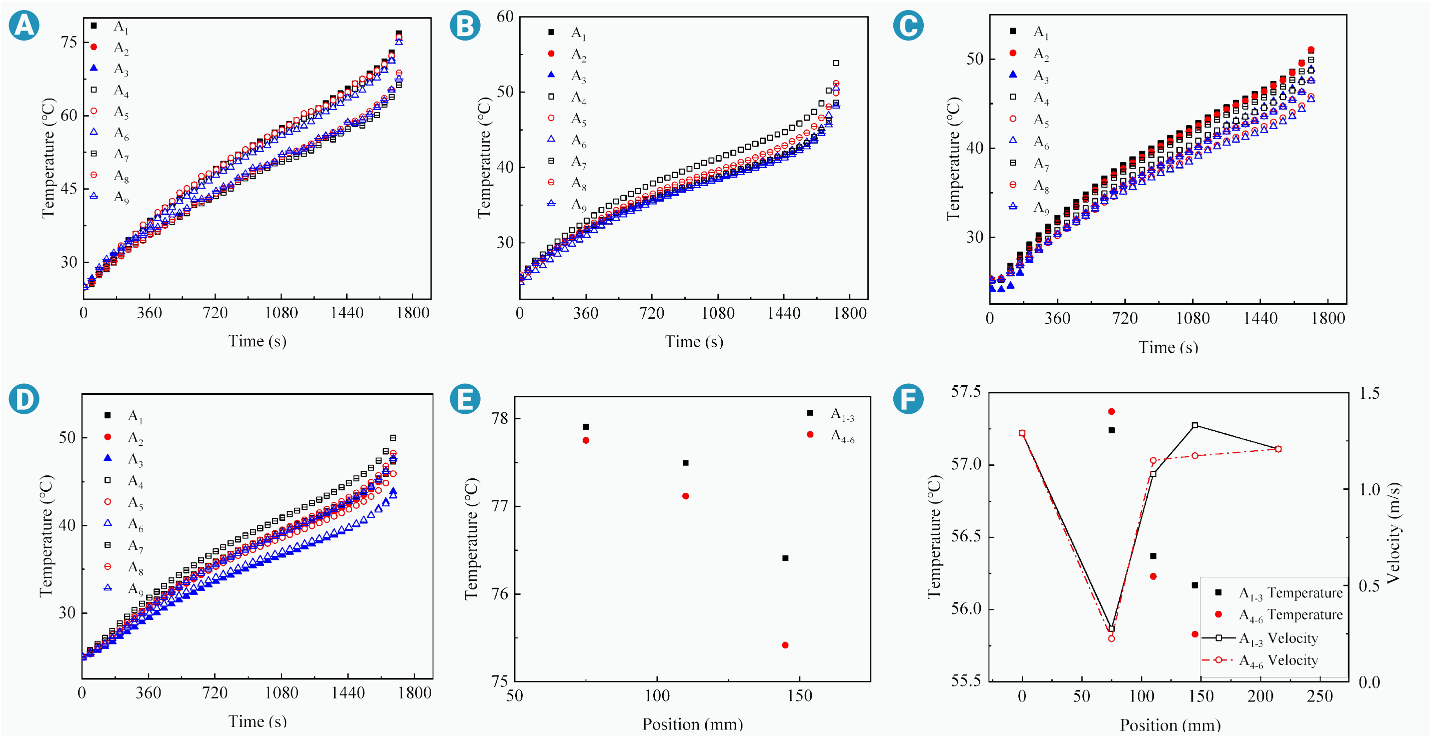

Figure 2. Temperature variations at each measuring point of 2C battery discharge experiments (A) Natural convection; (B) Air cooling; (C) Air-cooled coupled with PCM; (D) Air-cooled coupled with bionic PCM. Final temperature and velocity of each point at different positions of duct: (E) Natural convection of 2C discharge at A_1-A_6; (F) Air cooling of 2C discharge at A_1-A_6.

indicating that the polarization resistance of the battery is greater at both full charge and low charge states. This is consistent with the battery temperature rise observed in the experiment. The polarization voltage of high-rate discharge batteries is also higher than that of low-rate batteries, which explains why the heating of batteries is more intense at high rates.

Simulation verification

Mesh independence verification of single battery. Mesh independence verification minimizes the computational workload and time while preventing errors caused by an excessively coarse mesh. Through the experiments of battery, a simulation model for a single battery was developed for the mesh independence verification. The relevant parameters of materials of current model are shown in Table S4. A convection boundary condition was established on the outer surface of the battery, with the incoming flow temperature set at 25 °C. The coefficient of the convective heat transfer was computed using the UDF program. The time step was set to 1 s based on a sensitivity study, with a 100 maximum iterations per step. The residuals for the continuity equation and the velocity equation were set to 10^{-3}, while those for the energy equation were set to 10^{-6}. Similar to a previous study,[38] the number of mesh was 110 000, 260 000, and 570 000, respectively. A 2C discharge simulation was performed with different numbers of mesh, and the results of simulation are illustrated in Figure S8A. In consideration of the limitations of computational resources, a mesh size of 110,000 elements is chosen for the subsequent numerical simulations.

Given that the calculation of wall shear stress is required for the subsequent bionic structural design, and the accuracy of wall shear stress is highly depended on the mesh size of contact surface, a mesh independence verification of the wall shear stress was also performed for the battery coupled with air cooling and bionic PCM. In accordance with the previous study,[38] the mesh number of battery was set at 110 000, and the total mesh number of model was 940 000, 1 390 000, 1 820 000, and 2 650 000 respectively, where the bionic rib was thickened twice to make it denser. The results of simulation are shown in Figure S8B, and the mesh number of 1 820 000 for each battery is selected for the subsequent numerical simulations, while the same scheme of mesh is for the four batteries. All the mesh convergence results are listed in Table S5.

Temperature verification of mathematical model. Upon completion of mesh independence verification, various experimental configurations were established and corresponding simulations were performed. The simulated temperatures were then validated against battery discharge experiments. Figure 3A-D presents the comparison of the temperature curves of the simulated and experimental batteries at measuring points A_1-A_3 located at the 135° on the upper right battery under 2C discharge. The other data under 1C and 1.5C are listed in the attached Figure S9.

In order to evaluate the reliability of the developed model, the normalized mean bias error (NMBE) and the coefficient of variation of the root mean square error (CVRMSE) are adopted to compare the numerical and experimental results. Specifically, NMBE is used to measure the systematic deviation of the model, indicating whether the predicted values generally overestimate or underestimate the experimental data. Meanwhile, CVRMSE is applied to characterize the dispersion and consistency of the discrepancies between the predicted and measured values, thereby reflecting the robustness and predictive accuracy of the model. The mathematical expressions of NMBE and CVRMSE are given in Equations (18) & (19), respectively.

$$NMBE(\%) = \frac{\sum_i^n (T_{experiment} - T_{simulation})}{n \cdot \overline{T}_{experiment}} \times 100\% \tag{18}$$

$$CVRMSE(\%) = \frac{\sqrt{\left[\sum (T_{experiment} - T_{simulation})^2 / n\right]}}{\overline{T}_{experiment}} \times 100\% \tag{19}$$

As shown in Figure 3E, the NMBE and CVRMSE calculations indicate that the values for the 2C discharge are within the acceptable ranges of 5% and 15%, respectively, demonstrating that the simulated results align well with experimental data.

Table S6 summarizes the comparisons between the experimental and simulated data. The difference between experimental and simulated data increases with the increase of battery discharge rate, but the maximum average temperature difference of each group does not exceed 2 °C. The maximum temperature difference appears for natural convection battery at 2C discharge, and the difference between the experiment and simulation is 8.67%. However, during actual vehicle operation, the system would provide

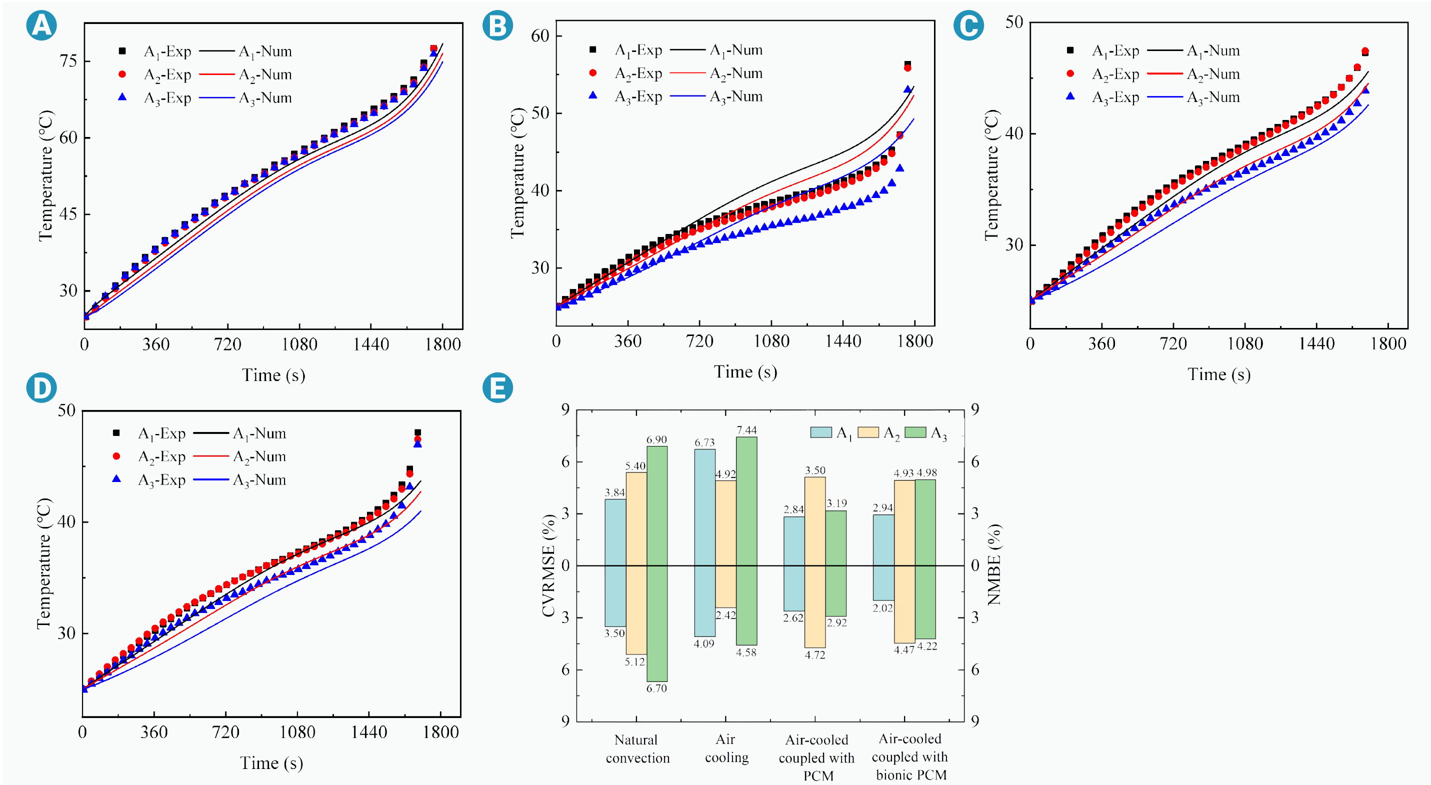

Figure 3. Verification of temperature of simulated model at 2C discharge (A) Natural convection; (B) Air cooling; (C) Air-cooled coupled with PCM; (D) Air-cooled coupled with bionic PCM. (E) Comparison of NMBE and CVRMSE between simulated and experimental temperatures

battery level protection, so generally there will be no over discharge of the battery, which has little impact on the simulation.

Pressure drop verification of mathematical model. The temperature verification of the model was followed by a simulation of the pressure difference between the duct inlet and outlet, which was then compared with experimental results for validation. The experiment measured the variation in inlet–outlet pressure difference during 2C discharge under three configurations, i.e., air cooling, air cooling coupled with PCM, and air cooling coupled with bionic PCM, were measured. Each measurement lasted 1800 s, with three repetitions for each configuration. The results are compared with the simulation outcomes, and the pressure difference are shown in Figure 4A-C and summarized in Table S3.

The observed fluctuations in Figure 4A-C are caused by the minor variations in the fan speed, sensor noise, and airflow instabilities, with a maximum variation of approximately ±0.1 Pa, which is consistent with the sensor accuracy. The averaging data are applied to clearly present the overall trend, but the underlying experimental data contain measurable fluctuations. The pressure difference between the inlet and outlet of the air duct slightly increases with the progress of the experiment. This is because the heat generated by battery discharge heats up the air around the battery, increasing the volume of air and leading to an increase in the pressure difference between the inlet and outlet. The simulated data of pressure difference is generally smaller than the experimental data, mainly due to the wiring of thermo-couples and imperfect sealing in the air duct during the experiment, which makes the experimental pressure difference larger. The data from multiple experiments shows that the pressure difference of bionic PCM is slightly smaller than that of smooth PCM, which is consistent with the simulation data results. The reduction in pressure drop provides an insight to reduce the fan power consumption in the larger scale application.

The temperature distribution and flow velocity distribution of smooth and bionic PCM under 2C discharge rate and 1.3 m/s flow velocity are shown in Figures 4D-G. Comparing Figure 4(D-II) with Figure 4(E-II), it can be seen that the temperature contour of the battery becomes light for bionic PCM, especially for upper left corner battery, indicating the heat transfer enhancement. Comparing Figure 4(F-II) and Figure 4(G-II), it is found that the velocity streamline becomes compact for the bionic PCM, which should benefit for the flow and heat transfer. The phonomenon can be attributed to the reduction of boundary layer for the bionic PCM.

Battery heat dissipation optimization

The preceding experiment examined the influence of duct configurations on battery temperature, and a CFD model was established, which was then validated against experimental data. In terms of optimizing the heat dissipation of bionic structures, in addition to relying on experimental data, the mechanism of heat dissipation enhancement would be deeply analyzed. Meanwhile, in response to the issue of excessive weight in bionic structures, the application of PCM in the preparation of bionic structures to reduce system mass and improve energy density would be explored. As a result, further optimized in terms of axial aspect ratio, lateral structure, rib row number, and rib arrangement are performed in the present study.

Following the model verification, a 2 × 2 × 2 battery pack was constructed. By the simulation results, the impact of the fish scale structure and its arrangement mode on the heat dissipation of the battery pack and the wind velocity at various positions within the duct would be explored. The battery pack model is shown in Figure 5A & B. Single battery is with the diameter of 46 mm, and the length of 80 mm. The duct size is 135 mm×135 mm× 301 mm, with the battery pack positioned at the center of the duct. Given that the battery pack is symmetrically distributed about the axis of the duct, the investigations of the temperature and velocity of the battery can be focused on the battery pack array. The model with an aspect ratio of 0.5 is used as an illustrative example, and the distribution of measuring points on the battery pack is shown in Figure 5A & B. On the surface of battery, the vertical axial direction and the right side of the front face are set as 0°. Temperature and velocity measuring points are arranged in the air and the surface of battery and its extension line at angles of 0°, 45°, 90°, 135°, and 315° in the clockwise direction. Additionally, in the axial direction of the battery pack, a total of 6 rows of measuring points are positioned at the surface of batteries.

Aspect ratio optimization. According to Bechert's theory,[34] the optimal size of concave parabolic ribs for drag reduction under different aspect ratios can be calculated based on the shear stress of a smooth surface at a given

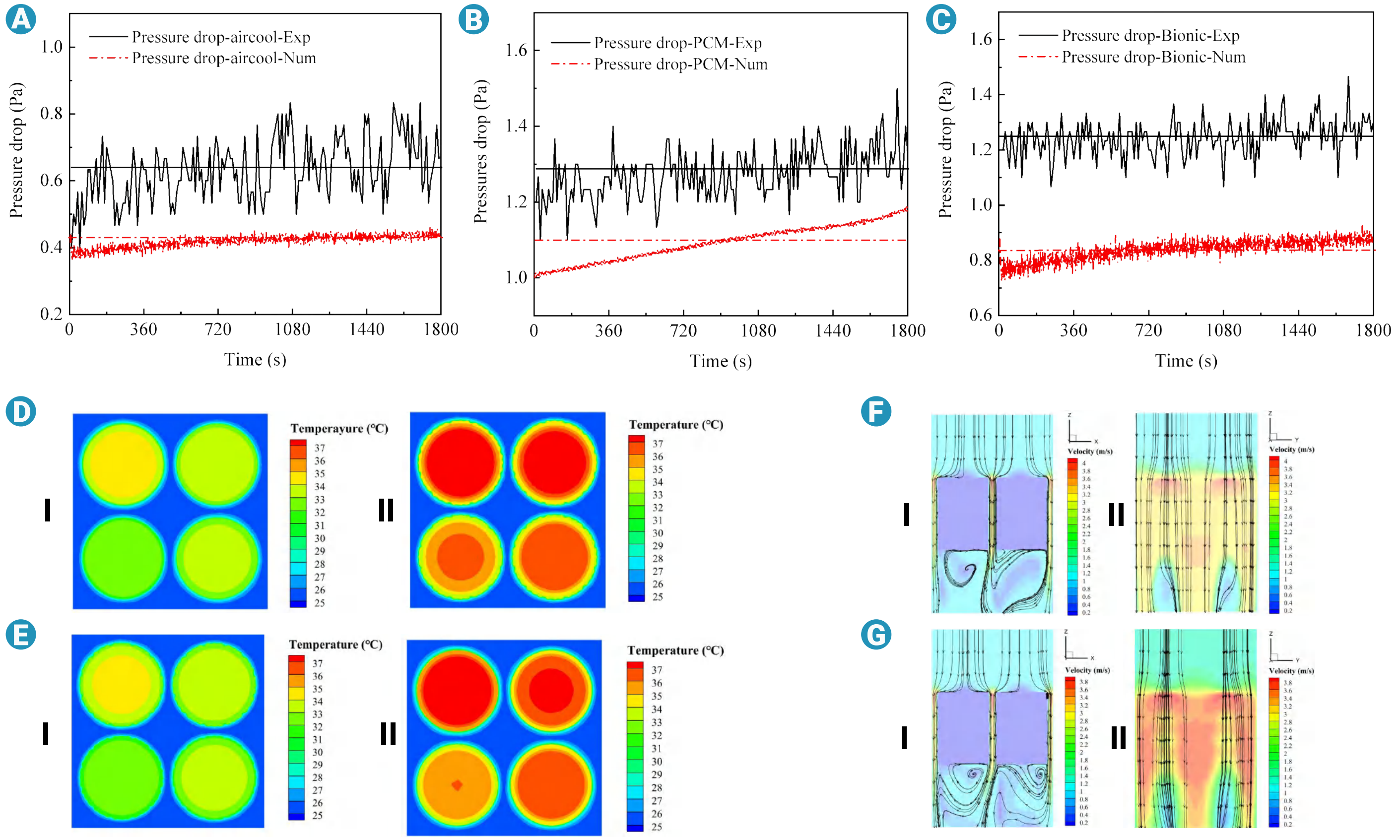

Figure 4. **Verification of pressure drop of simulated model at 2C discharge** (A) Air cooling; (B) Air-cooled coupled with PCM; (C) Air-cooled coupled with bionic PCM. Contours of temperature distributions with 2C discharge: (D) Air-cooled coupled with PCM; (E) Air-cooled coupled with bionic PCM. (I: 720 s; II: 1440 s). Contours of velocity distributions with 2C discharge in 1440 s: (F) Air-cooled coupled with PCM; (G) Air-cooled coupled with bionic PCM. (I: *xz*-direction; II: *yz*-direction)

wind velocity. Based on the approach, the optimal rib sizes corresponding to a wind velocity of 0.6 m/s are determined for aspect ratios of 0.5, 0.7, and 1.0. The calculated parameters are presented in Table S7. According to the calculated structural parameters, the optimal bionic scale size corresponding to the wind velocity of 0.6 m/s is drawn, as shown in Figure 5C-E.

The above three battery packs with different aspect ratios are modeled, and heat dissipation simulations are performed in Fluent. The simulation results are shown in Figure 6. Table S8 shows that the final temperature of the battery pack is lowest as 46.84 °C for the aspect ratio of 0.5, and highest as 47.08 °C for the aspect ratio of 1.0. As illustrated in Figures 6(A-I), (B-I), and (C-I), the highest temperature appears at the positive electrode, while the middle and negative electrodes exhibit the similar values, with the latter being slightly lower. The axial average temperatures at each point are comparable, and the maximum temperature difference within the battery pack is approximately 1.4 °C. Figures 6(A-II), (B-II), and (C-II) indicate that, except for the axial velocity at 135°, which increases continuously with the duct depth, the axial velocities at other angular positions decrease. At the positive electrode of the first battery, the wind velocity at 135° is not the highest, which is because the airflow, upon entering the narrow flow channel near the positive electrode, experiences strong disturbance at angles such as 0° and 90°, leading to locally increased velocities. As the airflow progressed downstream, the laminar sublayer near the channel wall thickens and the flow resistance increases, causing the airflow to converge toward the wider channel at 135°, where the velocity continues to rise.

Among the three models, the battery pack with an aspect ratio of 0.5 exhibits a higher axial wind velocity at 135° and a lower surface temperature. Therefore, the configuration with an aspect ratio of 0.5 is chosen for subsequent optimization.

Lateral structure optimization. Although the optimal aspect ratio of the shark-scale rib has been determined, the lateral profile of the original structure remains relatively simple and triangular. The sharp-edged profile might induce the local flow separation and additional transverse momentum loss when the airflow passes through the confined duct. Therefore, further optimization of the lateral rib profile is required. In the present study, the core bionic concept still originates from the shark-scale riblet structures, which regulate the near-wall flow and viscous sublayer. The nose profiles of high-speed train are not used as a direct analogy to train drag reduction under the open-air high-Reynolds-number conditions. Instead, they are introduced only as the representative streamlined geometries with smooth curvature and gradual cross-sectional variation. Such geometric features can help guide the local airflow around the rib surface, weaken the abrupt flow disturbance, and improve the compatibility between the rib structure and duct-confined airflow. Sun et al.[39] reported that different streamlined train nose profiles, such as the double-arch wide-flat shape, single-arch ellipsoid shape, and spindle shape with a front cowcatcher, can affect the aerodynamic resistance by regulating the boundary-layer development and lateral flow distribution.

According to the geometric rationale, lateral profiles of Fuxing bullet train of CR400AF, Fuxing bullet train of CR400BF and French TGV train were chosen to optimize the cross-sectional shape of the shark-scale ribs. Based on the aspect ratio of 0.5, the lateral structure of fish scale was optimized and designed. The relevant structures are shown in Figure 7A-C.

The above three battery packs with different lateral structures were modeled, and heat dissipation simulations were performed in Fluent. The simulation results are shown in Figure 7D-F. It can be seen from Figure 7D-F and Table S9 that the axial temperature distribution and wind velocity are similar to those in previous section. The final temperature of the battery pack with the lateral structure of CR400AF is the lowest at 46.24 °C, while that of the CR400BF is the highest at 46.94 °C. The maximum temperature differences of the CR400AF and TGV battery packs are about 1.2 °C, whereas that of the CR400BF is 1.4 °C. So, the axial velocities at 135° are comparable among the models. In conclusion, the CR400AF battery pack exhibits a lower surface temperature and a smaller maximum temperature difference of about 1.2 °C. Therefore, the model of streamlined structures of CR400AF is

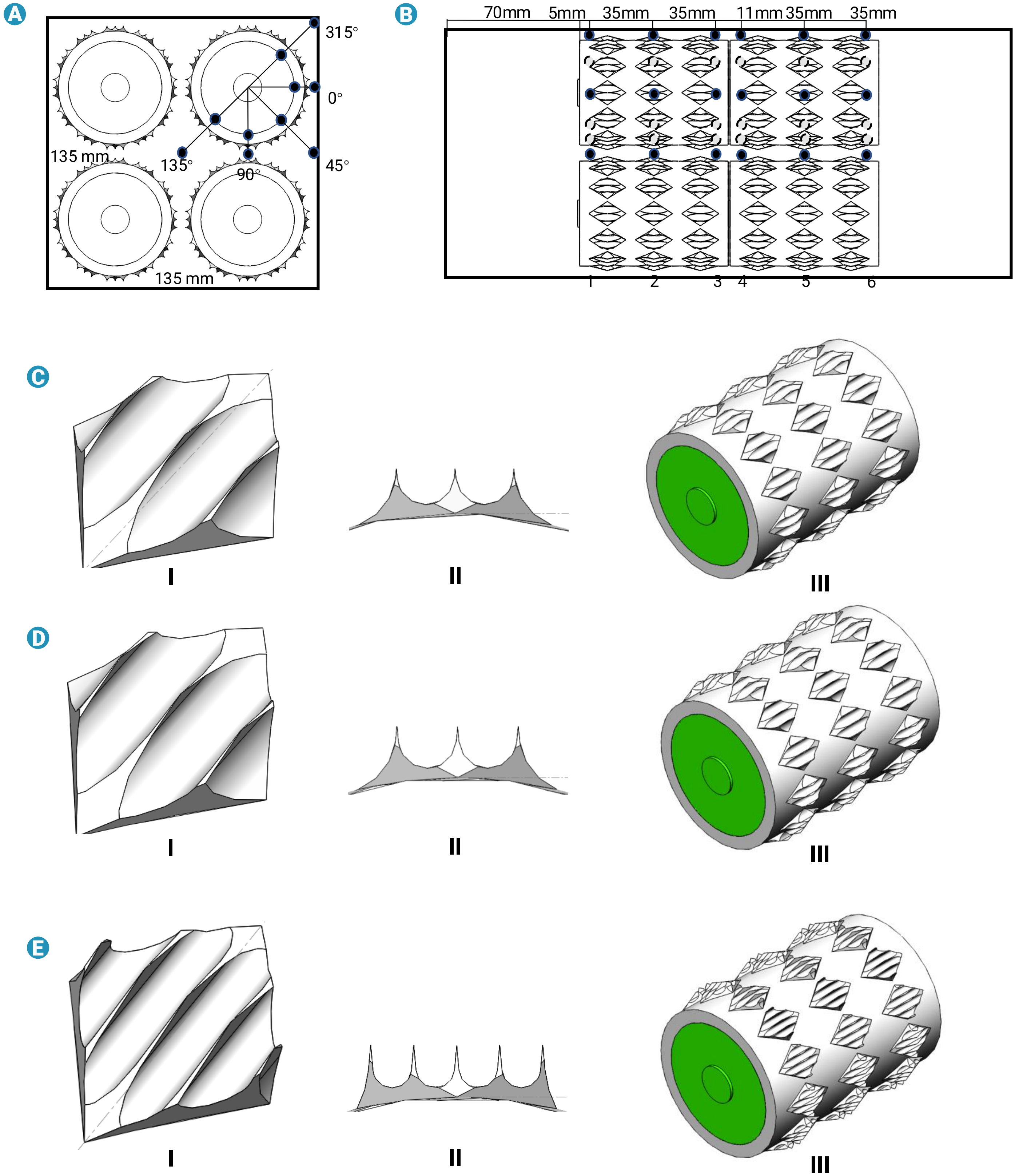

Figure 5. Schematic diagram of measurement points (A) Front view; (B) Side view. Rib optimization with different aspect ratios: (C) Aspect ratio of 0.5; (D) Aspect ratio of 0.7; (E) Aspect ratio of 1.0. (I: Full view; II: Front view; III: Battery covered with ribs.)

chosen for subsequent optimization.

Row number optimization. The existing models are all PCM coupled 12-row ribs for numerical simulation of heat dissipation. The influences of increasing or decreasing the number of rib rows on heat dissipation remain unclear. In the present study, models with 11 and 13 rib rows are designed as comparison groups in order to examine the effect of rib row number on the heat dissipation of battery performance and to identify the optimal configuration. By establishing the above three battery packs with different row number, the heat dissipation simulations are performed with Fluent. The simulation results are shown in Figure 8A-C. It can be seen from Figure 8A-C and Table

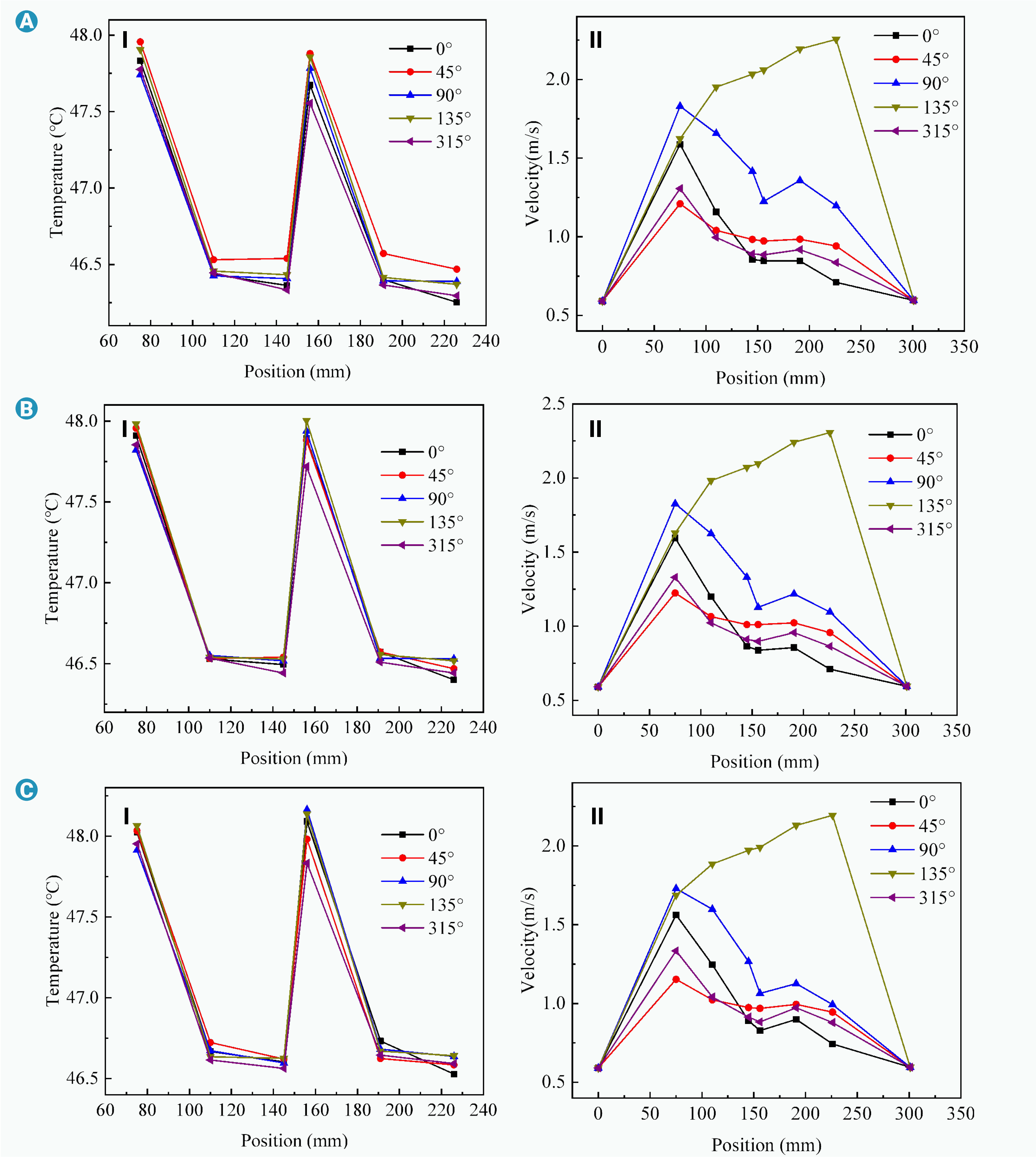

Figure 6. Simulation results of batteries with different aspect ratios (A) Aspect ratio of 1.0; (B) Aspect ratio of 0.5; (C) Aspect ratio of 1.0. (I: Battery final temperature; II: Wind velocity)

S10 that the axial temperature distribution, wind velocity are similar to those in previous two sections. In summary, the final temperature is the lowest of the battery pack with 13-row ribs, which is 46.18 °C, and the highest is the battery pack with 11-row ribs, which is 46.77 °C. The maximum temperature difference of the battery pack of 11-row is about 1.4 °C, while that of 13-row is 1.3 °C. The axial velocity of the 135° is similar. To sum up, the temperature of the battery pack of the 13-row ribs is lower, and the maximum temperature difference is about 1.3 °C. Therefore, the model of streamlined structures of 13-row ribs is chosen for subsequent optimization.

Arrangement mode optimization. The existing models are PCM coupled 13-row ribs, with the fish scales are arranged in a sequential row for numerical simulation of heat dissipation. As for the influence of the rib arrangement

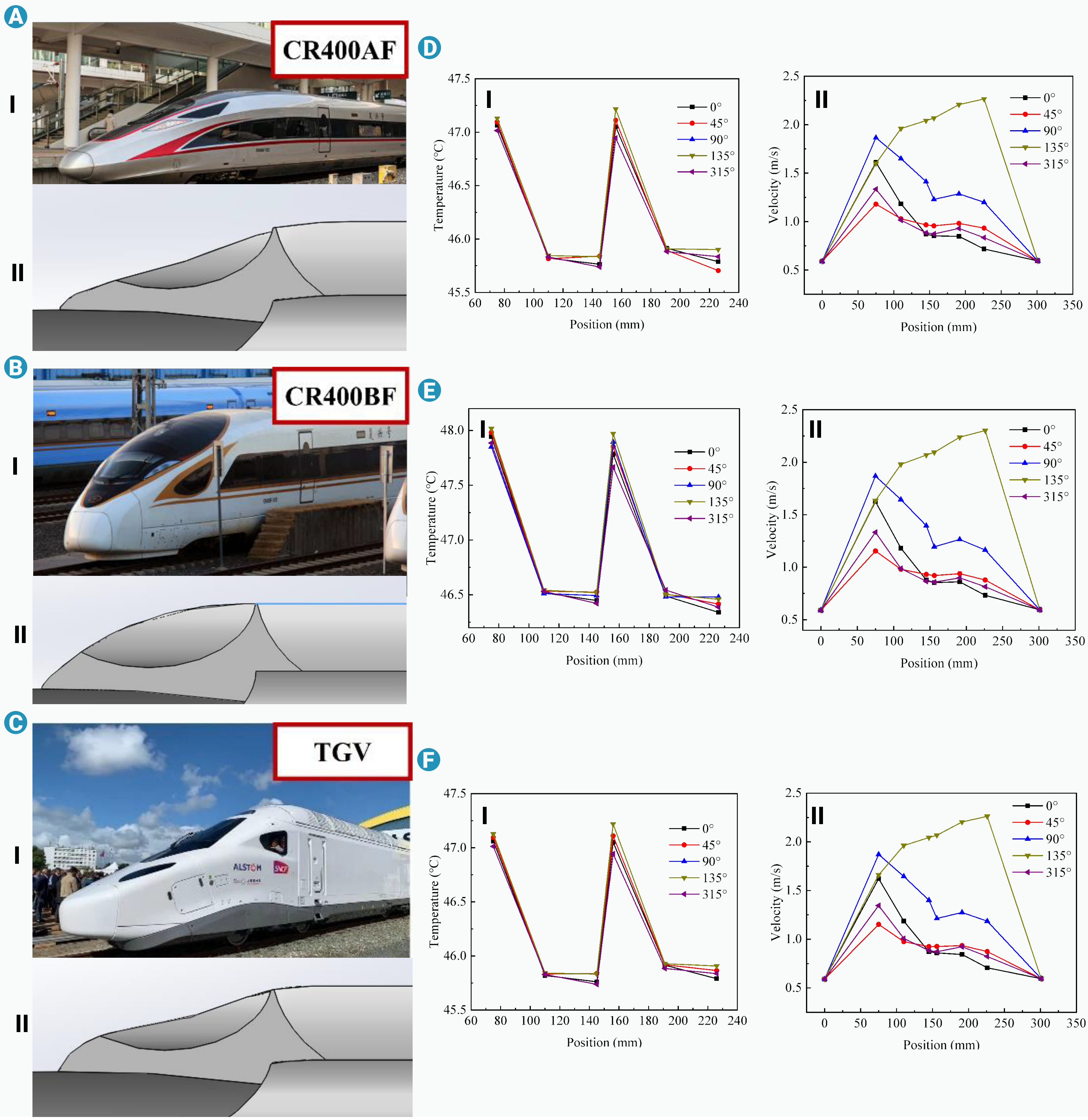

Figure 7. Rib lateral structure optimization (A) CR400AF; (B) CR400BF; (C) TGV train. Those train photos are from Internet. (I: Fuxing bullet train; II: Structure optimization.) Simulation results of batteries with different lateral structures: (D) Lateral structure of CR400AF; (E) Lateral structure of CR400BF; (F) Lateral structure of TGV. (I: Battery final temperature; II: Wind velocity)

on the heat dissipation is unclear. The model of 13 rows cross of ribs is designed as a comparison group to explore the influence of the rib arrangement on the heat dissipation of the battery. Two battery packs with different rib arrangements are established, and their heat dissipation performances are simulated with Fluent. The simulation results are shown in Figure 8D & E. It can be seen from Figure 8D & E and Table S11 that the axial temperature distribution, wind velocity are similar to those in previous section. The lower final temperature of the battery pack is with 13-row cross ribs, being 46.11 °C, and the higher is the battery pack with 13-row straight ribs, being 46.18 °C. The maximum temperature difference of the battery pack of straight is about 1.3 °C, whereas that of cross is 1.2 °C. The axial velocity at 135° is close to each other. The lower temperature of the battery pack with cross ribs is due to the cross-row structure inducing lateral eddy currents through lateral displacement, enhancing lateral thermal diffusion, essentially utilizing lateral forces. In all, the temperature of the battery pack of the 13-row cross ribs is lower, and the maximum temperature difference is about 1.2 °C. Therefore, the model of 13-row cross ribs is the optimal model obtained by

Through multiple simulation optimization, the optimal suitable structure and arrangement is obtained, with a fish scale aspect ratio of 0.5, a side structure of CR400AF, and 13 rows arranged in a cross pattern, as listed in

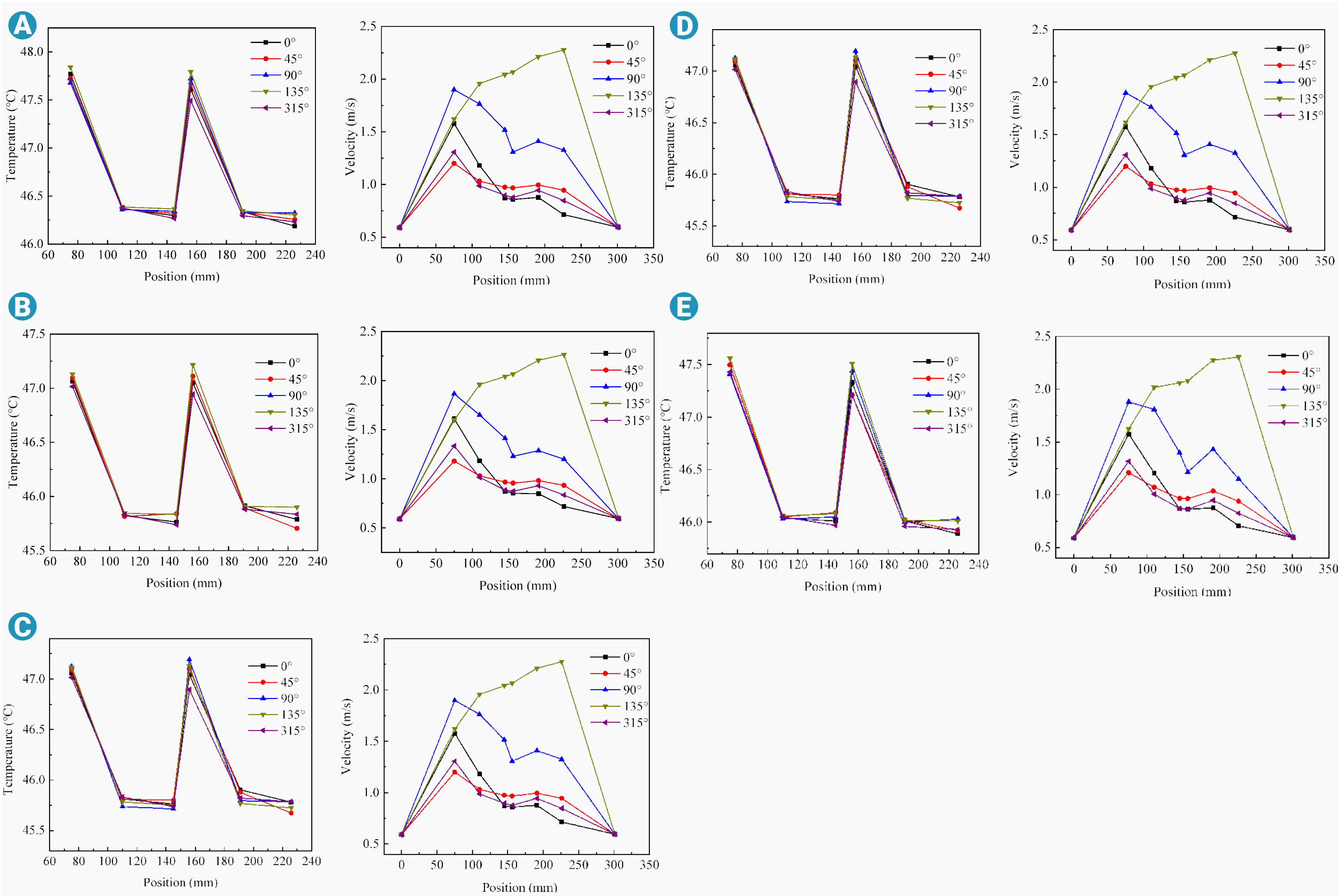

Figure 8. Simulation results of batteries with different row numbers (A) 11--row ribs; (B) 12--row ribs; (C) 13--row ribs. (I: Battery final temperature; II: Wind velocity). Simulation results of batteries with different 13-row rib arrangements: (D) Straight ribs; (E) Cross ribs. (I: Battery final temperature; II: Wind velocity)

Table S12. The average surface temperature of each point in the battery pack can be controlled at 46.11 °C, and the maximum temperature difference can be controlled at 1.2 °C.

Practical application and limitations

The proposed bionic PCM–air-cooled BTMS demonstrates strong potential for practical electric vehicle applications, particularly under moderate airflow conditions where traditional air cooling or PCM wrapping alone is insufficient. By combining the flexible composite PCM with bio-inspired surface structure, the system achieves effective thermal regulation while maintaining relatively low flow resistance. In addition, the bionic PCM heat sink can be fabricated using conventional compression molding techniques at the laboratory scale, with the main additional manufacturing requirement being a customized mold containing the shark-scale structure. Since the characteristic dimensions of the bionic geometry is at the millimeter scale, the proposed structure might be compatible with the scalable manufacturing processes such as mold pressing and hot embossing.

From an economic perspective, the material consumption is similar to that of conventional PCM wrapping, and the additional cost mainly arises from the initial mold fabrication. However, the practical manufacturing and application of the bionic PCM heat sink still require further evaluation. In the large-scale production, the consistency of rib morphology, mold precision, demolding reliability, and possible rib deformation during production should be carefully considered. In addition, the long-term shape retention of the bionic ribs under repeated melting–solidification cycles, mechanical pressure, vehicle vibration, and aging has not yet been verified. The thermal contact resistance between the PCM heat sink and battery surface might also change during the long-term operation. Therefore, although the proposed structure shows preliminary manufacturing feasibility, further thermal cycling tests, mechanical durability tests, and large-scale battery pack integration studies are required before the practical application in electric vehicle battery systems.

Nevertheless, several other limitations remain in the present study. The internal flow and natural convection of the melted PCM to improve the phase-change heat transfer model should be considered. The practical application requires a trade-off between the thermal regulation performance and system-level energy density as the PCM layer increases the weight of BTMS. The proposed system has only been verified at the laboratory scale, and long-term durability, vibration resistance, thermal cycling stability, airflow sensitivity, and large-scale battery pack integration have not yet been investigated. In addition, the optimization strategy adopted in current work is sequential rather than fully multi-objective. Although this approach can reveal the effects of individual geometric parameters, it might become inefficient when more design variables and operational conditions are considered.

CONCLUSIONS

Summary

In the present study, the bionic shark-scale-inspired composite PCM heat sinks integrated with axial air cooling are systematically investigated for lithium-ion BTMS. Rather than merely improving cooling performance, the role of bio-inspired surface structures in simultaneously regulating heat transfer and flow resistance in hybrid PCM–air-cooled BTMS is clarified. The main conclusions are summarized as follows:

(1) A synergistic regulation of heat transfer enhancement and flow resistance mitigation is achieved through the introduction of the bionic shark-scale PCM surface. Under a 2C discharge condition, the maximum battery surface temperature is maintained at 50.90 °C, corresponding to a 49.30% reduction in temperature rise compared with natural convection. Meanwhile, at an airflow velocity of 1.30 m/s, the duct pressure drop is reduced by 3.10%

relative to the smooth PCM configuration.

(2) Systematic parametric optimization demonstrates that the thermal–hydraulic performance of the bionic PCM surface is controlled by the coupled design of rib aspect ratio and lateral geometry. When the rib aspect ratio is set to approximately 0.5, effective matching between rib height and the local viscous sublayer thickness is achieved, which enhances the convective heat transfer without inducing a proportional increase in flow resistance. In addition, streamlined lateral rib profiles promote stable axial airflow and suppress transverse momentum dissipation, whereas less streamlined geometries generate stronger lateral disturbances. As a result of this combined geometric optimization, the CR400AF-inspired lateral structure achieved the lowest average battery pack temperature of 46.24 °C.

(3) Thermal performance is further improved through coordinated surface topology optimization rather than single-parameter adjustment. Increasing the rib row number to 13 and adopting a cross-arranged configuration redistribute the airflow more uniformly along the battery surface, thereby reducing local thermal accumulation. As a result, the lowest average battery pack temperature of 46.11 °C is obtained, accompanied by a maximum temperature difference of approximately 1.2 °C.

Future pespective

In future work, machine learning and AI-assisted optimization methods could be introduced to complement CFD-based simulations. For example, CFD results can be used to train surrogate models, such as response surface models, Gaussian process regressions, random forests, or neural networks, to rapidly predict the maximum temperature, temperature difference, pressure drop, and system weight under different bionic geometric parameters. These surrogate models can then be coupled with genetic algorithms, Bayesian optimizations, or multi-objective optimization methods to search a wider design space with lower computational cost.

Furthermore, it is indispensable to extend the present design to more demanding operational scenarios, including higher discharge rates and elevated ambient temperatures, to further evaluate the durability, reliability, and safety margins. The optimization framework should also be expanded toward multi-objective design by incorporating the thermal performance, pressure drop, system weight, manufacturability, and thermo-economic considerations. In addition, the proposed bionic PCM structure should be further explored in conjunction with liquid cooling or heat pipe-assisted configurations for high-power battery modules.

Nomenclature

A_1-A_9	Points for temperature measurement
C	Battery discharge rate
c	Coefficient of Nu calculation
c_p	Specific heat capacity (W·(m^2·K))
Gr	Grashof number
g	Gravity acceleration (m/s^2)
H	Total enthalpy (kJ)
h_{wall}	Battery natural convection coefficient (W/(m^2·K))
I	Electric current (A)
I_c	Electric current during charging (A)
I_{dc}	Electric current during discharging (A)
l	Battery length (mm)
L	Liquid phase fraction
M	Measurement accuracy
m	Mass (kg)
n	Coefficient of Nu calculation
Nu	Nusselt number
Pr	Prandtl number
P	Pressure (Pa)
ΔP	Pressure difference (Pa)
Q	Battery heat (W)
Re	Reynolds number
R_{ec}	Ohmic resistances during charging (Ω)
R_{edc}	Ohmic resistances during discharging (Ω)
R_{pc}	Polarization resistances during charging (Ω)
R_{pdc}	Polarization resistance during discharge (Ω)
S_T	Internal heat source (W)
s	Rib spacing (m)
s^+	Reynolds number of concave parabolic surface
T_0	Temperature with zero enthalpy (°C)
T_s	Freezing temperature of PCM (°C)
T_1	Melting temperature of PCM (°C)
t	Time (s)
u_τ	Wall friction velocity of smooth plate (m/s)
u^+	Dimensionless fluid velocity
V	Core volume of battery (m^3)
Δh	Height difference between longitudinal flow and transverse flow (m)
ΔV_{c1}	Charging ohmic voltage (V)
ΔV_{c2}	Charging polarization voltage (V)
ΔV_{dc1}	Discharging ohmic voltage (V)
ΔV_{dc2}	Discharging polarization voltage (V)
u,v,w	Velocity (m/s)
Greek symbols	
β	Volume expansion coefficient
γ	Latent heat (kJ/kg)
λ	Thermal conductivity (W/(m^2·K))
λ_{air}	Thermal conductivity of air (W/(m^2·K))
μ	Dynamic viscosity (N·s/m$^{2)}$
v	Kinematic viscosity (m^2/s)
ρ	Density (kg/m^3)
τ_0	Shear stress on concave parabolic plate (Pa)
$\Delta\tau$	Shear stress difference between concave parabolic plate and smooth plate (Pa)
Abbreviation	
BTMS	Battery thermal management system
DSC	Differential scanning calorimeter
HPPC	Hybrid pulse power characterization experiment
PCM	Phase change materials
SEM	Scanning electron microscope
SOC	States of charge
UDF	User defined function

REFERENCES

1. Zhao C., Yan J., Tian X., et al. (2023). Progress in thermal energy storage technologies for achieving carbon neutrality. *Carbon Neutral.* **2**:10. DOI:10.1007/s43979-023-00050-y
2. Eltoumi F., Becherif M., Djerdir A., et al. (2021). The key issues of electric vehicle charging via hybrid power sources: Techno-economic viability, analysis, and recommendations. *Renew. Sustain. Energy Rev.* **138**:110534. DOI:10.1016/j.rser.2021.110534
3. Xiao X. and Hui WX. (2026). Experimental and numerical study of a cascaded thermal energy storage system for waste heat recovery in hydrogen production plants. *Energy* **351**:140753. DOI:10.1016/j.energy.2026.140753
4. Xiao X., Yao MT., Xu YQ., et al. (2026). Preparation and characterization of TPEE@PEG1500/EG flexible composite phase change materials and thermal response for thermal management of batteries. *Energy Convers. Manag.* **352**:121044. DOI:10.1016/j.enconman.2026.121044
5. Zhang Y., Xie K., Shi J., et al. (2024). Dressing paraffin wax/boron nitride phase change composite with a polyethylene "underwear" for the reliable battery safety management. *Small* **20**:2304886. DOI:10.1002/smll.202304886
6. Shi R., Jiao S., Yue Q., et al. (2022). Challenges and advances of organic electrode materials for sustainable secondary batteries. *Exploration* **2**:20220066. DOI:10.1002/EXP.20220066
7. Yang F., Xie Y., Deng Y., et al. (2018). Predictive modeling of battery degradation and greenhouse gas emissions from US state-level electric vehicle operation. *Nat. Commun.* **9**:2429. DOI:10.1038/s41467-018-04421-8
8. Yang W., Zhou F., Zhou H., et al. (2020). Thermal performance of axial air cooling system with bionic surface structure for cylindrical lithium-ion battery module. *Int. J. Heat Mass Transf.* **161**:120307. DOI:10.1016/j.ijheatmasstransfer.2020.120307
9. Sur A., Narkhede S., Menon A., et al. (2024). Improving li-ion battery performance with internal cooling. *J. Adv. Res. Fluid Mech. Therm. Sci.* **125**:220–233. DOI:10.37934/arfmts.125.1.220233
10. Jouhara H., Serey N., Khordehgah N., et al. (2020). Investigation, development and experimental analyses of a heat pipe based battery thermal management system. *Int. J. Thermofluids* **1**:100004. DOI: Not retrievable. DOI:10.1016/j.ijft.2019.100004
11. Verma A., Shashidhara S. and Rakshit D. (2019). A comparative study on battery thermal management using phase change material (PCM). *Therm. Sci. Eng. Prog.* **11**:74–83. DOI:10.1016/j.ijft.2019.100004
12. Akinlabi A A H. and Solyali D. (2020). Configuration, design, and optimization of air-cooled battery thermal management system for electric vehicles: A review. *Renew. Sustain. Energy Rev.* **125**:109815. DOI:10.1016/j.rser.2020.109815
13. Kalaf O., Solyali D., Asmael M., et al. (2021). Experimental and simulation study of liquid coolant battery thermal management system for electric vehicles: A review. *Int. J. Energy Res.* **45**:6495–6517. DOI:10.1002/er.6495
14. Smith J., Singh R., Hinterberger M., et al. (2018). Battery thermal management system for electric vehicle using heat pipes. *Int. J. Therm. Sci.* **134**:517–529. DOI:10.1016/j.ijthermalsci.2018.08.038
15. Wu M., Li T., Wang P., et al. (2022). Dual-encapsulated highly conductive and liquid-free phase change composites enabled by polyurethane/graphite nanoplatelets hybrid networks for efficient energy storage and thermal management. *Small* **18**:2105647. DOI:10.1002/smll.2022.2105647
16. Shastri D., Mahajan M., Sur A., et al. (2025). Electric vehicle battery cooling using phase change materials and nanofluids. *Int. J. Heat Technol.* **43**:989–996. DOI:10.18280/ijht.430317
17. Sarkon G K., Hurdoganoglu D., Eyyamoglu B., et al. (2025). Preventing thermal runaway in lithium-ion batteries with nano-porous structures: A critical review. *J. Power Sources* **641**:236793. DOI:10.1016/j.jpowsour.2025.236793
18. Wu T., Wang C., Hu Y., et al. (2022). Research on novel battery thermal management system coupling with shape memory PCM and molecular dynamics analysis. *Appl. Therm. Eng.* **210**:118373. DOI:10.1016/j.applthermaleng.2022.118373
19. Safdari M., Ahmadi R. and Sadeghzadeh S. (2020). Numerical investigation on PCM encapsulation shape used in the passive-active battery thermal management. *Energy* **193**:116840. DOI:10.1016/j.energy.2020.116840
20. Alipanah M. and Li X. (2016). Numerical studies of lithium-ion battery thermal management systems using phase change materials and metal foams. *Int. J. Heat Mass Transf.* **102**:1159–1168. DOI:10.1016/j.ijheatmasstransfer.2016.1159
21. Choudhari V G., Dhoble A S. and Panchal S. (2020). Numerical analysis of different fin structures in phase change material module for battery thermal management system and its optimization. *Int. J. Heat Mass Transf.* **163**:120434. DOI:10.1016/j.ijheatmasstransfer.2020.120434
22. Wu W., Yang X., Zhang G., et al. (2016). An experimental study of thermal management system using copper mesh-enhanced composite phase change materials for power battery pack. *Energy* **113**:909–916. DOI:10.1016/j.energy.2016.07.090
23. Weng J., He Y., Ouyang D., et al. (2021). Honeycomb-inspired design of a thermal management module and its mitigation effect on thermal runaway propagation. *Appl. Therm. Eng.* **195**:117147. DOI:10.1016/j.applthermaleng.2021.117147
24. Lv Y., Liu G., Zhang G., et al. (2020). A novel thermal management structure using serpentine phase change material coupled with forced air convection for cylindrical battery modules. *J. Power Sources* **468**:228398. DOI:10.1016/j.jpowsour.2020.228398
25. Saleh R., Memarzadeh A., Hurdoganoglu D., et al. (2025). A comprehensive review on atomic layer deposition on key components in fuel cells. *Fuel* **395**:135172. DOI:10.1016/j.fuel.2025.135172
26. Sudo S., Tsuyuki K., Ito Y., et al. (2002). A study on the surface shape of fish scales. *Int. J. Ser. C Mech. Syst. Mach. Elem. Manuf.* **45**:1100–1105. DOI:10.1299/jsmec.45.1100
27. Zhang D., Luo Y., Li X., et al. (2011). Numerical simulation and experimental study of drag-reducing surface of a real shark skin. *J. Hydrodyn., Ser. B* **23**:204–211. DOI:10.1016/S1001-6058(10)60105-9
28. Oeffner J. and Lauder G V. (2012). The hydrodynamic function of shark skin and two biomimetic applications. *J. Exp. Biol.* **215**:785–795. DOI:10.1242/jeb.064837
29. Yang W., Zhou F., Chen X., et al. (2021). Performance analysis of axial air cooling system with shark-skin bionic structure containing phase change material. *Energy Convers. Manag.* **250**:114921. DOI:10.1016/j.enconman.2021.114921
30. Liu N., Jiang Y., Liu X., et al. (2025). Thermal performance analysis and structure optimization of bionic shark skin channel liquid cooling plate for lithium ion battery. *Appl. Therm. Eng.* **279**:127683. DOI:10.1016/j.applthermaleng.2025.127683
31. Xu WQ. (2025). Research on optimization of shark-like structure for flexible composite phase change materials and battery thermal management system coupled with air cooling. Master's thesis, Donghua University, Shanghai.
32. Lauder G., Wainwright D., Domel A., et al. (2016). Structure, biomimetics, and fluid dynamics of fish skin surfaces. *Phys. Rev. Fluids* **1**:060502. DOI:10.1103/PhysRevFluids.1.060502
33. Barai A., Uddin K., Widanage W D., et al. (2018). A study of the influence of measurement timescale on internal resistance characterisation methodologies for lithium-ion cells. *Sci. Rep.* **8**:21. DOI:10.1038/s41598-017-18123-8
34. Boomsma A. and Sotiropoulos F. (2016). Direct numerical simulation of sharkskin denticles in turbulent channel flow. *Phys. Fluids* **28**:035106. DOI:10.1063/1.4943434
35. Bechert D W., Bruse M. and Hage W. (1997). Experiments on drag-reducing surfaces and their optimization with an adjustable geometry. *J. Fluid Mech.* **338**:59–87. DOI:10.1017/S002211209700687X
36. Tao W. (2019). Heat Transfer. *Higher Education Press.*
37. Jiang CK., Wang JX., Yang LS., et al. (2026). Performance analysis of enhanced heat transfer in lithium-ion battery air-cooled thermal management systems coupled with vortex generators. *Int. J. Therm. Sci.* **227**:110903. DOI:10.1016/j.ijthermalsci.2026.110903
38. Xiao X. and Xu WQ. (2025). Optimal investigation on thermal management of battery based on biónical shark scale structure. *J. Refrig.* https://link.cnki.net/urlid/11.2182.TB.20251117.1526.003.
39. Sun Z., Yao S., Wei L., et al. (2021). Numerical investigation on the influence of the streamlined structures of the high-speed train's nose on aerodynamic performances. *Appl. Sci.* **11**:784. DOI:10.3390/app11020784

FUNDING AND ACKNOWLEDGMENTS

This work was sponsored by Key Laboratory of Advanced Technique & Preparation for Renewable Energy Materials (Grant No: MERE2024002), Shanghai Pujiang Program (Grant No. 20PJ1400200), Fundamental Research Funds for the Central Universities of China (Grant No. 2232021D-11), Shanghai Overseas High Level Talents Program.

AUTHOR CONTRIBUTIONS

All authors contributed to the manuscript and approved the final version.

DECLARATION OF INTERESTS

The authors declare no competing interests.

DATA AND CODE AVAILABILITY

Data are available from the corresponding author upon reasonable request.

SUPPLEMENTAL INFORMATION

It can be found online at: https://doi.org/10.59717/j.xinn-energy.2026.100182